

# The magnetic field of 4U 0115+63

Melanie Pfeuffer

*supervised by Prof. Dr. Jörn Wilms, Dr. Karl Remeis-Sternwarte,  
astronomical institute of the University Erlangen-Nürnberg*

(Dated: April 11, 2007)

In this project the RXTE observations of an outburst of the binary X-ray pulsar 4U 0115+63, having taken place in 2004 September–October, are analyzed with respect to luminosity-dependent cyclotron resonance energies and compared to an former outburst in 1999 March–April. It can be shown that both outbursts are subject to the same behavior relating to all considered characteristics.

## I. INTRODUCTION

Extraordinary importance has been attached to the study of the magnetic field of neutron stars. Since the magnetic flux is conserved during the collapse of the evolved progenitor star of the neutron star and the magnetic field strength is proportional to

$$B \propto R^{-3} \quad (1)$$

a rough estimate leads to  $B$ -field strengths from  $10^{12}$  G up to  $10^{14}$  G, which surpass the strongest magnetic fields obtained on earth a million times. Due to many observations and examinations it is known that these  $B$ -fields cannot decay spontaneously without external influences [1]. Though this is not valid for neutron stars in binary systems, where low magnetic fields have been observed in many systems. The reason therefore Geppert and Urpin (1994) suggested is accretion. Supposing a high enough accretion rate and further a long enough accretion phase, the neutron star is heated by the accretion which yields to a decreasing conductivity of the neutron star. Thus it follows that the magnetic field is also decreasing. Nevertheless there are also quite a few neutron stars in binary systems with an enormously high  $B$ -field in the range given above. This simply means that these neutron stars are too young in comparison to the time scale of magnetic field decay due to accretion, which direct one's attention to the accretion process in order to gain the time dependence of the  $B$ -field [1]. One of the methods of accurately measuring the present  $B$ -fields is analyzing the cyclotron resonance scattering features (CRSFs) in X-ray spectra since the line energy  $E_0$  of the fundamental CRSF is related to the magnetic field strength of the neutron star as

$$E_0 \sim 11.57 \text{keV} \cdot B_{12}, \quad (2)$$

whereas  $B_{12}$  is the magnetic field in units of  $10^{12}$  G. The relation (2) is known as '12-B-12 rule' and after taking gravitational redshift into account can be used to calculate magnetic field strengths [1].

In this project I consider a neutron star in a transient Be/X-ray binary system (see IV): the X-ray source 4U 0115+63 with 3.6 s pulsations [3] is an accreting X-ray pulsar, whose distance is estimated to 7 kpc. The companion is a 09e star V635 Cassiopeiae with an orbital

period of 24.3 days [3, 4]. Its CRSF were first discovered (1979) at  $\sim 20$  keV by Wheaton et al. (1979) in the HEAO-1 A4 spectra and later an additional CRSF was noted at  $\sim 12$  keV during the analysis of data from the lower energy HEAO 1/A-2 experiment by White (1979). Furthermore, Heindl et al. (1999) found for the first time in any pulsar a third harmonic feature in the HEXTE data of the outburst of 4U 0115+63 and were able to show that the line spacing between the fundamental and second harmonic as well as between the second and third harmonics are not equal and further not multiples of the fundamental line energy. Because of these earlier outbursts, the X-ray-spectrum of 4U 0115+63 was analyzed for several times and thus is one of the most suitable objects for studying the physics of cyclotron resonance in the polar caps of binary X-ray pulsars. Nakajima et al. (2006) reported on the luminosity-dependence of CRSFs, which was also discovered in the outburst in 1999 using RXTE data. These authors confirmed that the cyclotron resonance energy of 4U 0115+63 increases as the X-ray luminosity decreases, which might be a result of a decrease in the accretion column height. In this project, RXTE data of 4U 0115+63 covering an outburst in 2004 September–October are analyzed. The main task is once more to consider the resonance energy as continuous function of the luminosity. Hence one is able to decide whether the behavior of CRSFs in dependence of luminosity and thus accretion is the same compared with the former outburst in 1999 and so due to physical effects or whether a hysteresis effect can be detected.

The outline of the project is as follows: First a short insight in the scientific instruments, namely High Energy X-Ray Timing Experiment (HEXTE) and the Proportional Counter Array (PCA), aboard the Rossi X-Ray Timing Explorer (RXTE) the observations of the outburst were made with, is given. After that a rough insight in the topic of spectral fitting is given. Before attending to the basic theory of CRSFs in Sect. V the reasons as well as the mechanism of accretion are summarized. Then in Sect. VII C 1 I show that the behavior of the CRSFs during the outburst 2004 equals that one during the outburst in 1999 with respect to all considered characteristics.

## II. OBSERVATION WITH RXTE

Observations were made in both in the project considered outbursts (1999, 2004) with the Proportional Counter Array (PCA) and High-Energy X-ray Timing Experiment (HEXTE) on board RXTE.

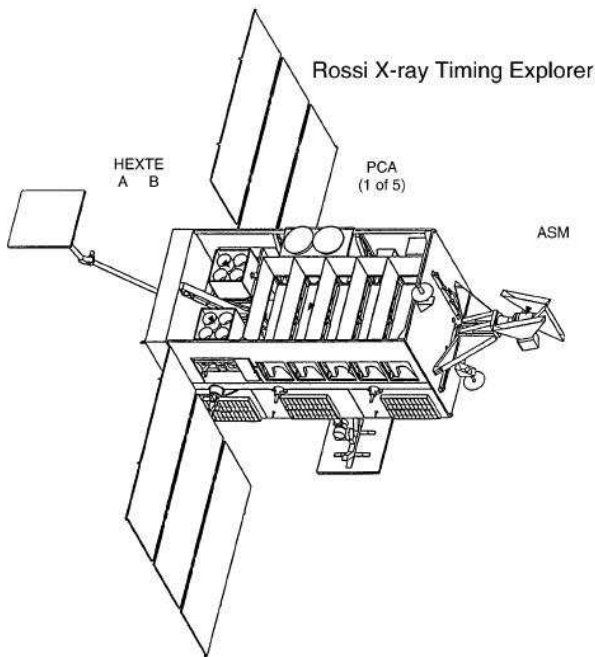


FIG. 1: RXTE spacecraft viewed from above. The five PCA proportional counters and the two HEXTE clusters A and B are shown, whereas on the front side the ASM lies [7]

### A. Instrument description

The Rossi X-ray Timing Explorer (RXTE) is a satellite, which was launched in 1995 December 30 by a Delta II rocket from the Kennedy Space Flight Center into a low earth orbit (LEO) with 580 km altitude and 23° inclination. Its orbital period is about 90 Minutes. RXTE was named after the astrophysicist Bruno B. Rossi, who worked in the field of solar X-ray emission [1]. RXTE contains three scientific instruments (see Fig. 1), namely

- the Proportional Counter Array (PCA; [8])
- the High Energy X-Ray Timing Experiment (HEXTE; [7])
- the All Sky Monitor (ASM; [9]).

Since many events like the outburst of transient X-ray pulsars cannot be predicted up to now, the ASM is of enormous advantage. It consists of three scanning shadow cameras (SSCs), which are independent. Each of the cameras has a field of view of  $90^\circ \times 6^\circ$  and stays in the same position for ninety seconds and then moves

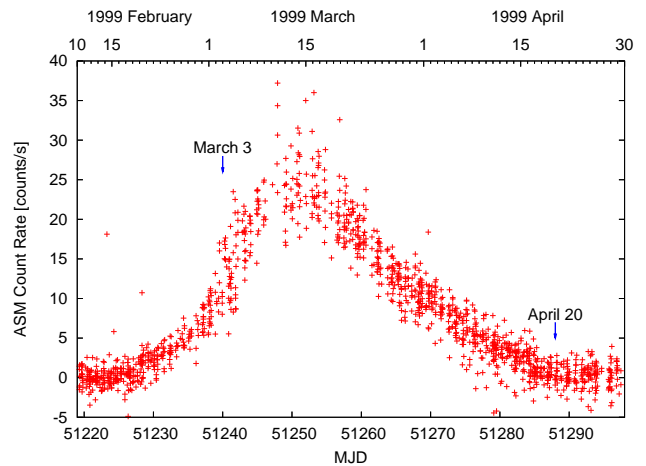


FIG. 2: RXTE/ASM light curve of 4U 0115+63 covering its outburst in 1999. The arrows indicate the first and the last spectrum observed with PCA and HEXTE (data from [10]).

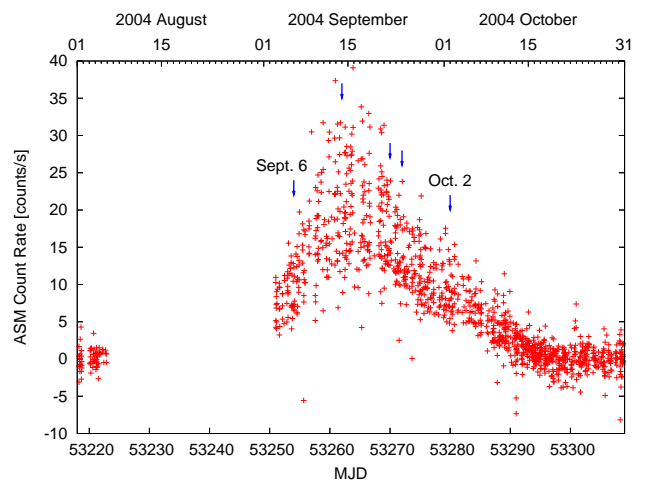


FIG. 3: RXTE/ASM light curve of 4U 0115+63 during its outburst in 2004. The arrows indicate the five with PCA and HEXTE observed spectra (data from [10]).

to a new position. Therefore  $\sim 80\%$  of the complete sky is scanned once a day. The ASM monitors the  $\sim 100$  brightest sources in the sky in the energy range from 2 to 12 keV. Whenever the ASM detects something unusual or of otherwise great importance (e.g. the outburst of 4U 0115+63 in 1999 March, see its lightcurve in Fig. 2), it is possible to abort the current observation and point the satellite to the interesting position in less than one hour, since RXTE's high slewing speed of  $\sim 6^\circ/\text{minute}$ . The only exceptions are areas next to the sun, since these endanger the instruments, which for example Fig. 3 shows during almost the whole August. Then in the week August 27 – September 2 the intensity suddenly rose to  $\sim 65$  mCrab and in the following week up to  $\sim 190$  mCrab so that one could be sure to observe an outburst. Consequently it was decided to take five accurate measurements of the radiation of 4U 0115+63 (the first one taking place in September 6, also see Fig. 3).

TABLE I:  
RXTE observations of 4U 0115+63 in the 2004 September–October outburst

Date (2004)	PCA		HEXTE
	PCU No.	Exposure (ks)	Exposure (ks)
Sept 6	0, 2	1.60	0.83
Sept 14	0, 1, 2, 3	0.59	0.75
Sept 22	0, 2	16.8	13.6
Sept 24	0, 2	3.49	2.26
Oct 2	0, 2, 3, 4	3.44	2.32

For such pointed observations are the two other scientific instruments responsible. In order to obtain the detection of the energy range as broad as possible, in RXTE from 2 keV to over 200 keV, PCA is sensitive at lower energies (2–60 keV), while HEXTE is in charge of radiation at higher energies (15–250 keV).

The PCA consists of five xenon proportional counters units, called PCUs. Its total effective area is  $\sim 6000 \text{ cm}^2$  if all PCUs are operating. Since soon two of the five PCUs, later followed by the other three, showed improper behavior including breakdowns, they were periodically switched off in order to let them rest. So it is common practice to use just a few of the five PCUs for observations. Thus during the detection of the outburst of 4U 0115+63 in 1999 only in eleven out of 34 PCA observations on different days all PCUs were operating simultaneously [3]. Table I shows the observing PCAs during the 2004 outburst of 4U 0115+63. After voltage changing in 1999, also in order to extend the lifetime, the PCA has now a nominal energy range from 2 to 100 keV. However the useful energy range is between 2 keV and 30 keV, because on the one hand the Xenon K edge at 34.6 keV reduces the effective area strongly, while on the other hand the response matrix for energies in the range above the the Xenon K edge is not well understood, although the effective area has increased up to  $1000 \text{ cm}^2$  again. Fig. 4 illustrates the efficiency of both of the instruments PCA and HEXTE. The Xenon K edge can be seen very well. Also one recognizes that above 20 keV HEXTE is the more appropriate instrument. The HEXTE consists of two independent arrays of detectors, cluster A and B. Each of them contains four NaI(Tl)/CsI(Na) phoswich scintillation counters, sensitive in an energy range of 15 – 250 keV. All eight detectors are coaligned on source to gain together a  $1^\circ$  FWHM field of view and a total net open area of  $\sim 1600 \text{ cm}^2$  [7]. However early in the mission one of the four detectors of clusters B failed, so the effective area of cluster B is reduced by  $\sim 25\%$ . One task to solve was the high background of the detectors compared to PCA. Therefore the method of Source Beam Switching is used and thus an almost real-time estimate of the background is possible. The HEXTE cluster rocking subsystem changes the orientation of the cluster between on- and off-source posi-

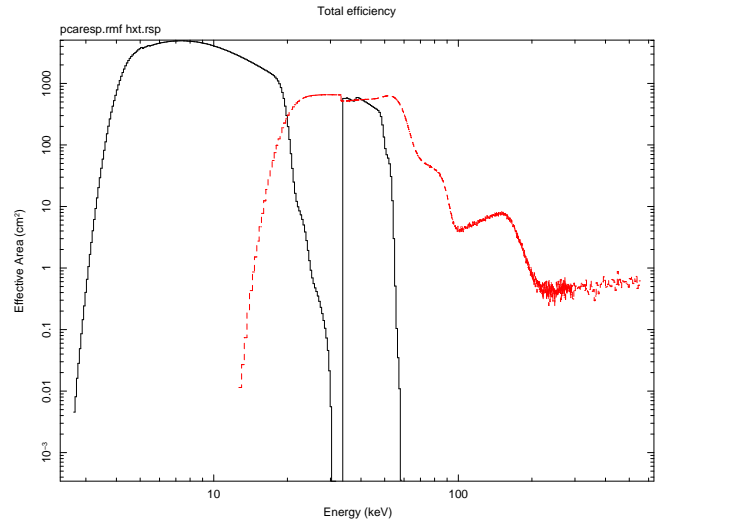


FIG. 4: The two graphs show for the effective area ( $\text{cm}^2$ ) versus energy (keV) of the two instruments, PCA (black) and HEXTE (red). The data are obtained by the PHA files of an observation of 4U 0115+63 in 2004-09-14.

tion every 32 s. Since the rocking axes of the cluster A and B are adjusted orthogonal to each other, four background regions are available. In order to interpret the shape of the effective area of HEXTE in dependence of the energy (once more see Fig. 4) one has to know that at lower than 20 keV photoelectric absorption takes place in the housing above the detector, whereas at higher energies finite NaI(Tl) thickness yields reduction of the effective area. Interesting are also the sharp drops around 30, 60, 100 and 110 keV. So for example that one near 30 keV is due to the change in photoelectric cross section at the K edge of iodine.

Considering the effective areas of both instruments PCA and HEXTE and taking only the ranges with high effective areas I have chosen to use PCA data in the energy range from 4 keV up to 20 keV and HEXTE data in the range 20–60 keV for analysis of the spectra.

Moreover one big problem every kind of satellites but especially X-ray satellites are confronted with are the radiation and particle belts around the earth. Thus RXTE is in general lucky to be launched into LEO and therefore far below the radiation belts in the altitude of about 1000 km, called 'van Allen belts' resulting from the specific configuration of the magnetic field. However there still remains one position in the south Atlantic south-east off the coast of Brazil, known as the South Atlantic Anomaly (SAA, see Fig. 5), where the configuration of the magnetic field of the Earth distinguishes. While high energy particles usually cannot leave the van Allen belts, due to a dent in the magnetosphere above this area they can enter this zone. Thus in order to protect the detectors from the very intense particle background the RXTE has even to be shut off during its passing through the SAA-zone. Furthermore after the satellite has left the

SAA the 25 minute half-life radioactive decay of  $^{128}\text{I}$  results in an exponential decrease of additional background radiation, which is evident for about half of its orbit [1, 7].

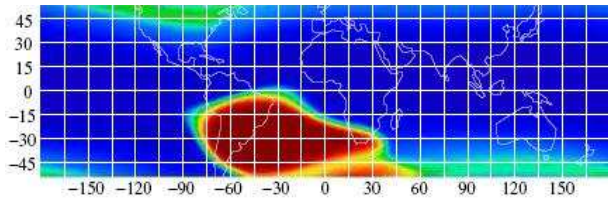


FIG. 5: South Atlantic Anomaly (SAA) in the south Atlantic southeast off the coast of Brazil (from [1])

### III. SPECTRAL FITTING AND XSPEC

#### A. The basics of spectral fitting

Life would be easy if the detectors of RXTE are able to supply people on earth with the real spectrum of the source. However, this isn't possible as it requires an unequivocal identification between each single energy of the incoming radiation and detector channel. Instead we have to take for a fix photon energy the probability for each channel to detect this photon into consideration. Therefore one introduces the function

$$R(I, E) \quad (3)$$

called instrumental response, which is as mentioned above proportional to the probability that an incoming photon will be detected in channel  $I$ . Of course the instrumental response (3) is tried to be found out accurately before missions in laboratories, but at the latest problems arise if some detector devices have failed during mission or parameters are changed to values, that have not been tested before (as the voltage change in the PCUs of the PCA).

Then the detector counts in dependence of each channel  $I$ ,  $C(I)$ , is obtained by integration of the spectrum of the source  $f(E)$  weighed with the instrumental response  $R(I, E)$  over all energies:

$$C(I) = \int_0^{\infty} f(E)R(I, E)dE \quad (4)$$

Mathematically, knowing  $C(I)$  and  $R(I, E)$ , an inversion of equation (4) yields the wished spectrum  $f(E)$ . Unfortunately the problem is not unique in general. Thus one has to go the other way round: Suggest a model for the spectrum  $f(E, p_1, p_2, \dots)$ , which is usually dependent on several parameters  $p_1, p_2, \dots$ , and calculate due to (4) a predicted count spectrum  $C_p(I)$ . Then compare it to  $C(I)$  and test whether the model "fits" the data. In order to judge the goodness of a fit, usually  $\chi^2$  is used as fit statistics:

$$\chi^2 = \sum (C(I) - C_p(I))^2 / \sigma(I)^2, \quad (5)$$

where  $\sigma(I)$  is the error for channel  $I$ , estimated by  $\sqrt{C(I)}$ . After varying the parameters one obtains a best fit due to (5). These parameters are called *best fit parameters* and consequently its model *best fit model*. The  $\chi^2$  statistics provides a generally accepted goodness-of-fit criterion for a given number of degrees of freedom  $\nu$ , which is equal to the difference between the number of channels and the number of model parameters. One wants the reduced  $\chi_{\text{red}}^2$ ,

$$\chi_{\text{red}}^2 = \chi^2 / \nu \sim 1. \quad (6)$$

So a reduced  $\chi^2$  much greater than 1 shows that the fit isn't good enough, while a reduced  $\chi^2$  much smaller than 1 is a sign for overestimated errors of the data [11].

#### B. A short description of spectral fitting with XSPEC

XSPEC is a command-driven, interactive X-ray spectral-fitting program (for a more detailed description see [11]). The software was developed with the additional constraint to be completely detector-independent. The challenge was to provide an algorithm finding the best fit parameters in a short time as possible. For the search of the best fit parameters the Levenberg-Marquardt-algorithm (see [12]) is used, which solves minimization problems. It combines the Newton-Gauß-algorithm with a regulation technique that forces the function, which has to be minimized, to decrease in each step. Thus the procedure converges even with worse starting parameters in comparison to the Newton-Gauß-algorithm, but instead convergence speed decreases. However, having reached a local minimum once, there is absolutely no chance to reach the global minimum. Hence one has to estimate the starting parameters in the surrounding of the global minimum in order to get the global minimum, which is assumed to yield the correct scientific parameters.

### IV. ACCRETION IN X-RAY BINARIES

#### A. Accretion

As it is generally known the energy source of a neutron source is accretion, which is by the way the most efficient way (at least for neutron stars) to gain energy from a particle with a certain mass. For this the companion in the binary is of big importance. Having two stars in a binary with masses  $M_1, M_2$  each of them contributes a gravitational potential to the total potential, known as *Roche potential* in a co-rotating frame of reference, whereas the stars are considered as point masses. This yields 5 Lagrange points (see in Fig.6  $L_1-L_5$ ) and the inmost equipotential surface encompassing both stars, called *Roche surface*, in which all gravitational forces nullify. Thus whenever material of the companion crosses

the Roche surface it can be accreted by the neutron star or expelled into interstellar medium. Due to the release of potential energy accretion of material with mass  $m$  therefore results in an energy gain  $\Delta E_{acc}$  of

$$\Delta E_{acc} = \frac{GMm}{R_{NS}} = \eta mc^2, \quad (7)$$

with  $\eta = \frac{GM}{R_{NS}c^2}$ .  $M$  designs the neutron star mass and  $R_{NS}$  is its radius. Taking typical values,  $M = 1.4M_{\odot}$ ,  $R_{NS} = 10$  km, leads to  $\eta = 0.2$ . Therefore the energy release for the accretion of one electron is calculated as 100 keV. So energy of this order at the surface of the neutron star is converted into radiation (X-rays) or it is used to heat the surrounding material.

In principal there are three methods the optical companion can donate material to the neutron star, which are introduced in the following.

- *Roche Lobe Overflow*

Due to stellar evolution the optical companion will expand and once exceed its Roche volume (see again Fig. 6). As already discussed above, then the mass outside of the Roche surface isn't bound to the companion any more and thus can be accreted by the neutron star. However, the angular momentum of the material is too big for the possibility to accrete the material directly. Instead, an accretion disk forms. In this disk collisions take place and a part of the material escapes while the other part loses step by step its angular momentum such that it moves further inwards. Consequently, the density in the disk grows with decreasing radius. Friction due to viscosity on the one hand supports the loss of angular momentum and thus the movement inwards

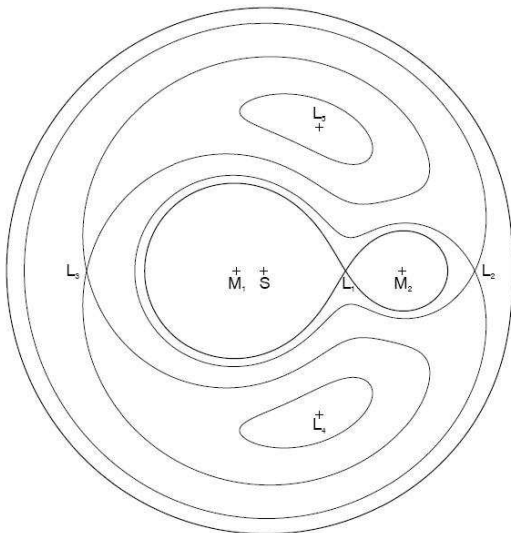


FIG. 6: In the Fig. (from [1]) are shown the equipotential surfaces of the Roche potential. Of special interest is the *Roche surface*, the inmost equipotential surface encompassing both stars.

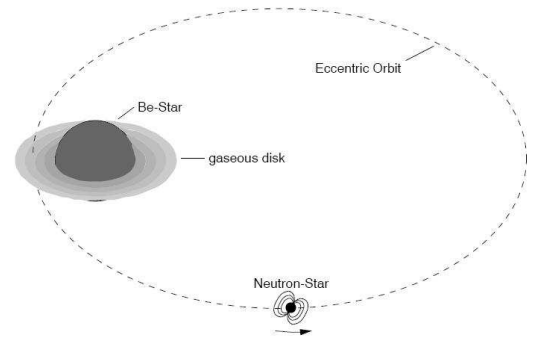


FIG. 7: A neutron star in an eccentric orbit around a Be star. 4U 0115+63 belongs to the transient Be/X-ray binaries, in which X-ray outbursts only can be observed after the accretion disk of the neutron stars has filled by mass transfer during periastron passages. Otherwise luminosity is too low to be observed. Figure from [1].

and on the other hand yields high temperatures in the inner parts of the disk.

- *Be Mechanism*

Before explaining the accretion mechanism of Be binaries it is reasonable to give a short insight in the development of Be/X-ray binaries, especially since 4U 0115+63, which is of main interest in this project, belongs to these binaries.

Be/X-ray binaries are the result of the evolution of a binary system of two B-stars, whereas the resulting neutron star has been the more massive star initially. First the progenitor of the neutron star donates mass by Roche Lobe Overflow (cf. IV A) onto its companion due to hydrogen-shell-burning, which is resulting in a helium star orbiting a Be-star. Since the transferred material also inhabits angular momentum, the angular momentum is also transferred and consequently the companion rotates faster, it is *spun up*. This, by the way, is assumed to be the reason for the formation of a decretion torus around the companion. Then again the helium-star transfers mass onto its companion, due to a similar process, namely helium-shell-burning until it undergoes a supernova explosion finally. Losing mass and experiencing a velocity kick during the supernova explosion can lead to wide eccentric orbits (see in Fig.7)[13].

Due to these wide orbits the neutron stars in a Be binary are not able to accrete material from their companions, whenever they are far away from the Be-star. Accretion only takes place when the neutron star approaches periastron and enters the decretion torus around the Be-star (illustrated in Fig.7). Once the accretion disk of the neutron star has filled during the passage, material is accreted onto the neutron star, the released energy is converted at least partly to X-rays and thus an X-ray

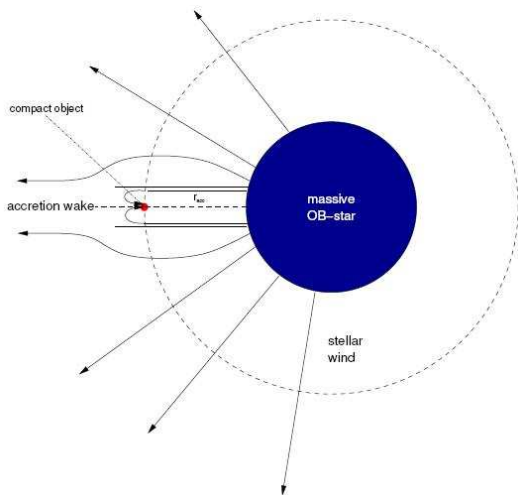


FIG. 8: Accretion from the companion onto the compact object (neutron star) via stellar winds. It can be seen clearly how deep the object is embedded in the wind. In Be/X-ray binaries this accretion method becomes important outside the periastron. Figure from [1].

outburst can be observed. Having left the accretion torus again, mass transfer is aborted. For a short time the accretion disk is able to sustain accretion onto the neutron star but soon the luminosity will decrease and stay at a very low level until the next periastron passage. Thus outbursts arise in such systems due to their orbital period.

However, one can imagine systems, called *transient sources*, which are so dim outside periastron, such that they are hardly observable. One prominent example is once again 4U 0115+63. In some cases it can even happen that though a periastron passage has taken place, no X-ray outburst can be observed. The reason for this behavior is assumed to be that the Be-star has lost its torus, and consequently is unable to transfer mass onto the passing neutron star.

- *Stellar Wind*

Since all stars have weak stellar winds, the third method for accretion remains for discussion: accretion via stellar wind. In case of O or B stars being the optical companions the stellar wind can be very intense. Knowing the fact that a neutron star usually passes its companion with a distance of less than one stellar radius (measured from surface to surface), it is obvious that the neutron star is really embedded in the stellar wind (see Fig. 8). In Be/X-ray binaries this accretion method is also attached importance, since outside periastron mass transfer can be obtained by stellar wind and thus remain observable.

Assuming accretion as single energy source the energy gain depends only on the amount of accreted material

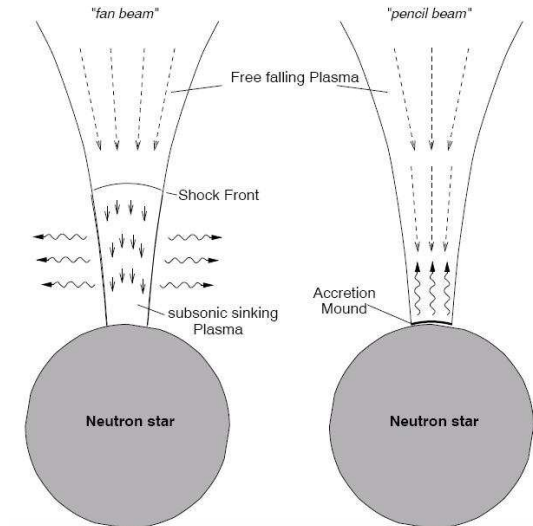


FIG. 9: One hat to distinguish between low (right) and high (left) accretion rates onto neutron stars: while at low accretion rates the infalling plasma simply falls onto the surface, at high accretion rates the plasma is decelerated or even stopped due to photon-electron interactions as well as Coulomb-forces (electrons-protons). Figure out of [1]

per time,  $\dot{M}$ . However, once a certain intensity of resulting radiation is reached, one can no longer ignore the pressure of the outgoing radiation since Thomson scattering becomes more and more important for the electrons. Although due to the low cross section Thomson scattering for protons is still negligible, the protons stay at the electrons because of Coulomb forces. With increasing luminosity the radiation pushes more and more against the infalling material and a shock front is forming (see Fig. 9). At a certain luminosity, the *Eddington Luminosity* the impact of the radiation pressure and the gravitational forces are in equilibrium and the following equation is valid:

$$GMm_p = \frac{L\sigma_T}{4\pi c} \quad (8)$$

$$L_{edd} = 4\pi GMm_p c \sigma_T \quad (9)$$

$$\approx 1.3 \times 10^{38} \frac{M}{M_\odot} \text{ergs}^{-1}, \quad (10)$$

whereas  $m_p$  is the proton mass ( $m_p \gg m_e$ ). However, in the ansatz above (8) a spherically symmetric accretion was assumed. With the accretion taking place only in a fraction  $f$  of the whole surface, the maximum luminosity is also reduced to  $f \cdot L_{edd}$ . But this relation is again not valid if the accretion area gets too small. Then the radiation is able to escape sideways and thus the pressure on the infalling material is reduced. Therefore the flux even can be *Super-Eddington* locally.

## B. Accretion geometry

Since we know that in binary systems a procedure of mass transfer exists and that first this material is deposited to the accretion disk and then accreted, we can have a more detailed look on the mechanism of accretion. Here the fact becomes important that the neutron star is not only a very compact object, but also exhibits a strong magnetic field. Thus mass that's going to be accreted, not simply falls onto the neutron star surface, after having lost its angular momentum due to friction. Instead, it is influenced in the vicinity of the neutron star by the magnetic pressure  $P_{mag}$ , which can be stated as at a radius  $r$ :

$$P_{mag} = \frac{\mu^2}{8\pi r^6}, \quad (11)$$

where  $\mu$  is the magnetic moment and the magnetic field geometry of the neutron star is assumed to be equal to dipole geometry with

$$B \sim \frac{\mu}{r^3}. \quad (12)$$

At a certain radius, the *Alfvén radius*  $r_m$  or also known as *magnetospheric radius* (see Fig. 10), the magnetic pressure and the ram pressure of the infalling material will be equal [1]:

$$\frac{\mu^2}{8\pi r_m^6} = \frac{(2GM)^{1/2} \dot{M}}{4\pi r_m^{5/2}} \quad (13)$$

Using (13) one can calculate the Alfvén radius for a typical neutron star:

$$r_m = 2.9 \times 10^8 M_1^{1/7} R_6^{-2/7} L_{37}^{-2/7} \mu_{30}^{4/7} \text{ cm} \quad (14)$$

Mass at this radius is forced to follow the magnetic field lines and thus it is accreted onto one of the poles of the neutron star and therefore an *accretion column* arises.

However, today one is not sure about the geometry of the accretion column, whether it is a hollow or a "solid" cylinder. Moreover its structure depends on the accretion rate, what is discussed later (in section VI).

## V. CRSF FORMATION

The best way to obtain information about the geometry of the accretion column is the analysis of Cyclotron Resonance Scattering Features (CRSF). The CRSFs are absorption features in X-ray spectra of accreting neutron stars that arise due to high magnetic field strengths of the order  $B \sim 10^{11} - 10^{13}$  Gauss. There is a lot of literature concerning the physics of charged particles in magnetic fields (e.g. , Harding and Lai, 2006) and thus only the most important relations are presented afterwards. Due to quantum mechanics the motion of the electrons (e.g. , Landau and Lifshitz, 1977) perpendicular to the

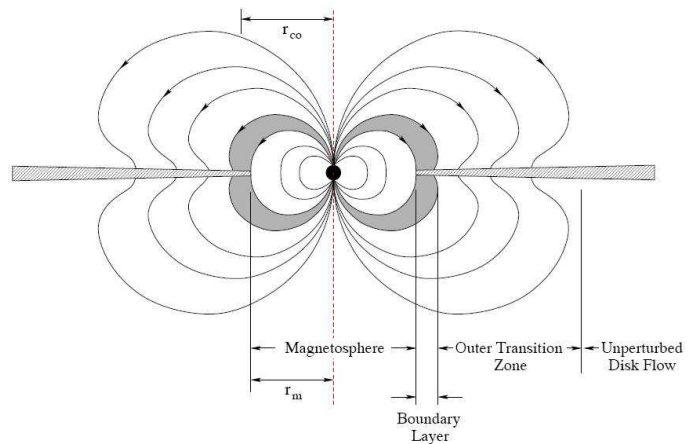


FIG. 10: At the Alfvén radius  $r_m$  the magnetic field gets so strong, such that the material of the accretion disk has to follow the magnetic field lines. Figure from [1].

magnetic field is quantized. Thus the energy of a free electron with the momentum  $p_{\parallel}$  is quantized in *Landau levels* and can be obtained by solving the Dirac Equation (e.g. , Johnson and Lippmann, 1949):

$$E_n = m_e c^2 \sqrt{1 + \left(\frac{p_{\parallel}}{m_e c}\right)^2 + 2n \frac{B}{B_{\text{crit}}}}, \quad (15)$$

where  $n$  is an positive integer number and  $B_{\text{crit}} = (m^2 c^3)/(e\hbar)$  is the critical magnetic field strength. A relativistic treatment yields Landau levels that are not equidistant. Furthermore the angle between the magnetic field and the path of photon  $\theta$  is of importance:

$$E_n = \frac{m_e c^2}{\sin^2 \theta} \left( \sqrt{1 + 2n \frac{B}{B_{\text{crit}}} \sin^2 \theta} - 1 \right) \quad (16)$$

Due to the energy gain by accretion, photons arise from the X-ray emitting region interact with the electrons. The quantization of the electron energies results in the photon absorption of discrete energies that raises the electrons exactly from into a higher Landau level. In the case of  $B \ll B_{\text{crit}}$  using Taylor expansion of (15) the energy difference  $E_{\text{cyc}}$ , that turn out to be equally spaced, between two Landau levels can be calculated:

$$E_{\text{cyc}} = \frac{\hbar e B}{m_e} \quad (17)$$

Inserting the constants in (17) leads to the popular '12-B-12 rule' (see (2)) which is an important result since it connects the fundamental cyclotron line energy with the strength of the magnetic field of the neutron star.

The location of the line forming region is unknown but assumed to be close to the surface of the neutron star, since high magnetic field strengths are required. Thus gravitational redshift has to be considered, which is at the neutron star surface approximately

$$z = \frac{1}{\sqrt{1 - \frac{2GM}{Rc^2}}} - 1 \quad (18)$$

Taking typical neutron star parameters again, a redshift of  $z \sim 0.3$  is derived [17].

As one knows from observational studies, the second harmonic is generally deeper than the fundamental line. Furthermore, the profile of the fundamental line is clearly non-Gaussian, but sometimes features like emission wings occur. Schoenherr et al. (2007) developed a convolution model to simulate the fundamental line in dependence of different parameters like the optical depth and temperature and compared it to results from observational data analysis [17].

## VI. CYCLOTRON EMISSION IN DEPENDENCE OF ACCRETION

As it was shown in Sect. V in eqs. (15),(17) the cyclotron line energies depend directly on the magnetic field. Since the magnetic field strength is changing with the distance between the electrons and the neutron star (NS) according to (12), the cyclotron line energy  $E$  in the approximation of  $B \ll B_{\text{crit}}$  depends on the height  $h_r$  of the line forming region as  $E \sim (R_{\text{NS}} + h_r)^{-3}(1+z)$ , where  $R_{\text{NS}}$  is the radius of the NS and  $z$  the gravitational redshift (18). Neglecting the radius dependence of  $z$ , the relation between  $E$  and the cyclotron line energy  $E_0$ , obtained directly on the NS surface, can be stated as  $(E/E_0)^{-1/3} = 1 + h_r/R_{\text{NS}}$ . Consequently one obtains

$$\frac{h_r}{R_{\text{NS}}} = \left(\frac{E}{E_0}\right)^{-1/3} - 1. \quad (19)$$

Thus knowing  $E$  from spectral analyzing and an estimate of  $E_0$  yields the relative height of the line forming region. Of course, the height of this region also depends on the amount of plasma being accreted per time. So again the point is reached, where one has to distinguish the case in which the plasma directly falls on the surface of the NS (sub-Eddington accretion) and when the local Eddington rate exceeds a certain value interactions between the emerging radiation and the infalling plasma can not be neglected any more (super-Eddington accretion). Here the decisive parameter that already was discussed in IV A is the local Eddington luminosity given by (see [18])

$$L_E = \frac{2\pi G M c m_p}{\sigma_T} \left(\frac{\sigma_T}{\sigma_m}\right) \theta_c^2 \simeq 10^{36} \text{ erg/s} \left(\frac{\sigma_T}{\sigma_m}\right) \left(\frac{\theta_c}{0.1}\right)^2, \quad (20)$$

where  $M$  is the NS mass (again assumed to be  $1.4M_{\odot}$ ) in the numerical estimation,  $\sigma_m$  is the photon-electron scattering crosssection in the magnetic field,  $\sigma_T$  is the Thomson crosssection and  $\theta_c$  represents the half-opening angle of the polar cap magnetic field lines. Since Staubert et al. (2007) suggested transient pulsars (as 4U 0115+63) to have evidence for a transition from super- to sub-Eddington accretion these different accretion regimes are of extraordinary interest for this project. The aim of the following two sections is to introduce simple models for

the accretion procedure for each of the two cases that yield relationships between the altitude of the line forming region and the luminosity. Since the luminosity  $L$  can be calculated by means of the measured flux according to

$$L = \text{flux} \cdot 4\pi R^2, \quad (21)$$

where  $R$  is the distance between the observer and the NS (in case of 4U 0115+63 approximately 7kpc), it is possible to compare the theoretical models to observed data.

### A. Sub-Eddington accretion

A low-luminosity accretion model was introduced by Nelson et al. (1993). It is assumed that the accretion beam enters the atmosphere at free fall velocity, such that the kinetic energy is given by the release of potential energy according to (7). The atmosphere is modeled as an electron-proton plasma with a magnetic field in the  $\hat{z}$  - direction. Thus the accreting ions entering the atmosphere are interacting with the plasma and lose energy to atmospheric electrons via magnetic Coulomb collisions and exciting the plasma to plasma oscillations. However, one must also consider the impact of the magnetic field. As it is shown in [18] the primary effect of the field is to reduce the plasma stopping power, since the transfer of proton energy to electron motion perpendicular to the magnetic field is suppressed. In order to find a relationship between the position of the line forming region and the luminosity, one starts with a Taylor expansion of (19) using  $r = R_{\text{NS}} + h_r$  and arrives at  $\Delta r/R_{\text{NS}} = -1/3 \Delta E/E$ . Staubert et al. (2007) identified  $h_r$  with the characteristic braking length for protons  $l_*$ , which itself can be estimated by the mean free path  $l_* \sim 1/n_e \sigma$ , such that now  $r = R_{\text{NS}} + l_*$ . Using the last relation and the density dependence of  $l_*$  one gets  $\Delta r/l_* = -\Delta n_e/n_e$  and consequently one obtains

$$\frac{\Delta r}{R_{\text{NS}}} = -\frac{1}{3} \frac{\Delta E}{E} = -\frac{l_*}{R_{\text{NS}}} \frac{\Delta n_e}{n_e}. \quad (22)$$

So a relation between the electron density and the luminosity has to be found. Nelson et al. (1993) determined the electron density  $n_e$  with the assumption of a neutral electron-proton plasma by hydrostatic equilibrium  $P = 2n_e kT = gy$ , where  $P$  is pressure,  $T$  temperature and  $y$  the mass column density. Staubert et al. (2007) extended the model by considering also the dynamical pressure of accreting protons. The dynamical pressure of the infalling protons, which can be obtained from Euler-Equation, was added to the hydrostatic term  $P = gy + (\rho_0 v_0^2 - \rho v^2)$ . Staubert et al. (2007) considered the different terms more closely and finally obtained for the electron density  $n_e \simeq (\dot{M}/A)(v_0/2kT)(\tau/4\tau_*)$  ( $A$  is the accretion area for one pole,  $\tau$  is the Thompson optical depth and  $\tau_*$  is the proton stopping depth) such that

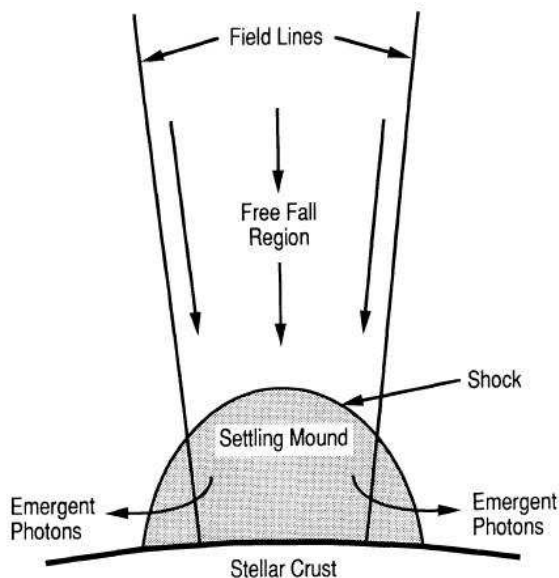


FIG. 11: The figure (from [20]) shows the free falling plasma. It is decelerated in such a strong way that it is transformed into subsonically settling plasma by the shock. Emerging photons are able to escape sideways.

eq. (23) becomes

$$\frac{\Delta r}{R_{\text{NS}}} = -\frac{1}{3} \frac{\Delta E}{E} = -\frac{l_*}{R_{\text{NS}}} \frac{\Delta \dot{M}}{M} = -\frac{l_*}{R_{\text{NS}}} \frac{\Delta L}{L}. \quad (23)$$

### B. Super-Eddington accretion

In contrast to low-luminosity accretion the radiation pressure dominates the deceleration of the infalling plasma in the super-Eddington radiation regime, what results in the formation of a shock front above the NS surface. This radiation-dominated shock transforms the free falling plasma into the subsonically settling plasma of the mound (see Fig. 11) [20]. Moreover, the accretion column has more cylindrical geometry, since the emerging photons escape from the sides of the mound [14, chap 11]. Burnard et al. (1991) studied this dynamical model in detail and found for the relative height of the peak of the mound the estimation

$$\frac{h_{\text{top}}}{R_{\text{NS}}} \approx \frac{L}{L_{\text{edd}} H_{\parallel}} \quad (24)$$

Here,  $H_{\parallel}$  denotes the ratio of the Thomson cross section to the Rosseland averaged electron scattering cross section for radiation flow along the magnetic field. A typical value for an ordinary NS is  $H_{\parallel} = 1.23$ , which is also used in the theoretical estimation of the height of the line forming region later.  $L_{\text{edd}}$  is given by (8).

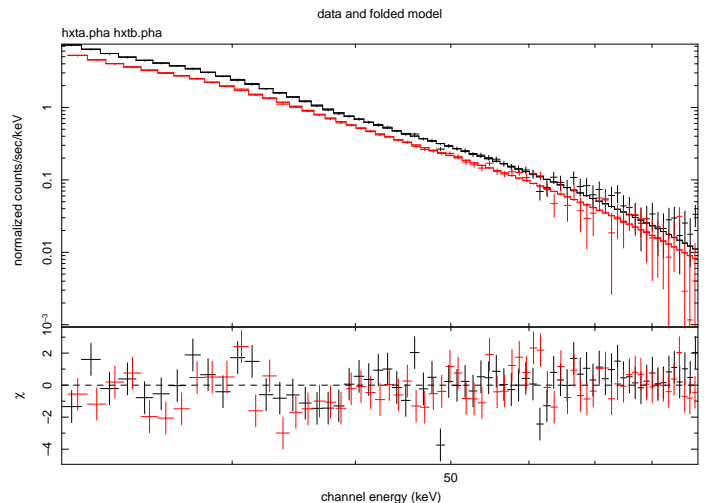


FIG. 12: Data of HEXTE cluster A and B of the observation in 1999 March 5. Fitting both data with the chosen model yields same residuals, what justifies to add the data of both arrays of detectors. One sees also in the upper part of the figure that HEXTE B has a lower effective area, since one of its four detectors failed already (see again chap. II A).

## VII. ANALYSIS AND RESULTS

In this section the behavior of the CSRF energy of the 2004 Sept–Oct outburst of 4U 0115+63 is analyzed. The chosen model is tested before by using it for the 1999 March–April outburst that has already been studied by Heindl et al. (1999) and Nakajima et al. (2006). Heindl et al. (1999) discovered a third CSRF in the spectrum in a narrow phase range and detected a non-equally spacing of the CSRFs. Furthermore, these people concluded

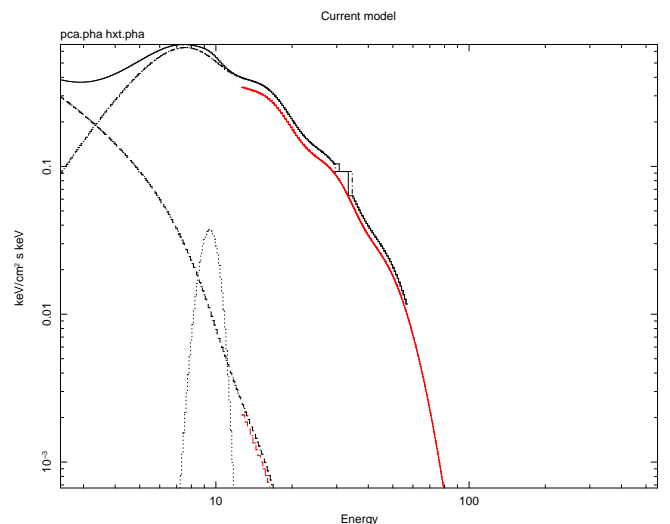


FIG. 13: An example for the resulting model the data (here 1999-03-20) are fitted with.

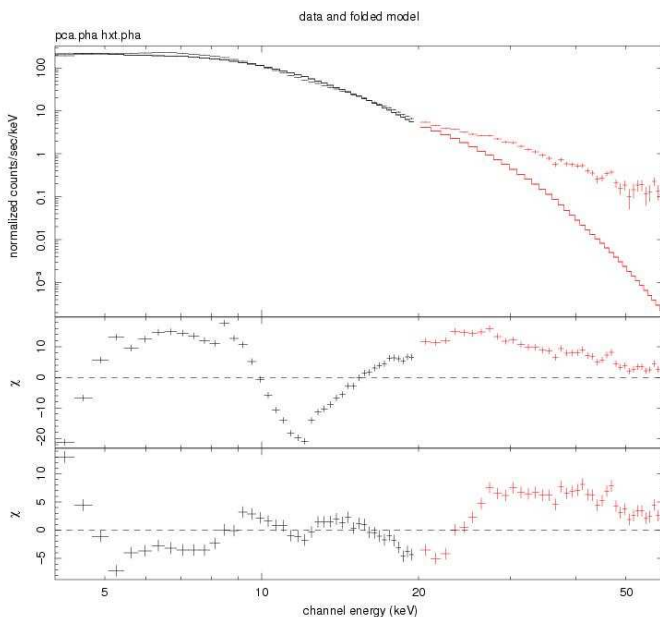


FIG. 14: *Top*: The figure shows the pointing observation data of 1999-03-20, compared with the folded model after fitting the continuum model. *Middle*: Note that the huge residuum near 10 keV indicates the fundamental cyclotron line. *Bottom*: Big improvement is achieved when fitting with the fundamental cyclotron line around 10 keV. However, new residuals around 20 keV arise that give rise to a second CRSF.

from a strong variability of the continuum and CRSFs with pulse phase a complex emission geometry near the neutron star polar cap. Nakajima et al. (2006) utilized the pulse-phase averaged data of this outburst and found luminosity-dependent changes of the cyclotron resonance energies. This dependence was interpreted as change in the accretion column height. Like Nakajima et al. (2006), in this project only pulse-phase averaged data were considered. First the data of HEXTE cluster A and B were compared and it was shown that by fitting a continuum model with two gaussian absorption lines that represent the fundamental and the 1st harmonic CRSF (see Fig. 12), residuals appeared at the same positions. Thus in the following analysis the data of cluster A and B were added and analyzed together. Furthermore the PCA and HEXTE data were fitted simultaneously with the same model besides a constant factor to equalize the relative normalizations. This factor was in both outbursts out of the range (0.8 : 1.4) and in most spectra close to 1.0.

### A. Spectral Models

The calculation of the the emission of a accretion powered neutron star is because of its complex geometry quite complicated. As was suggested by several people (see [1, chap 5.3.1]), the dominating process is assumed to be *resonant Compton scattering*, what results

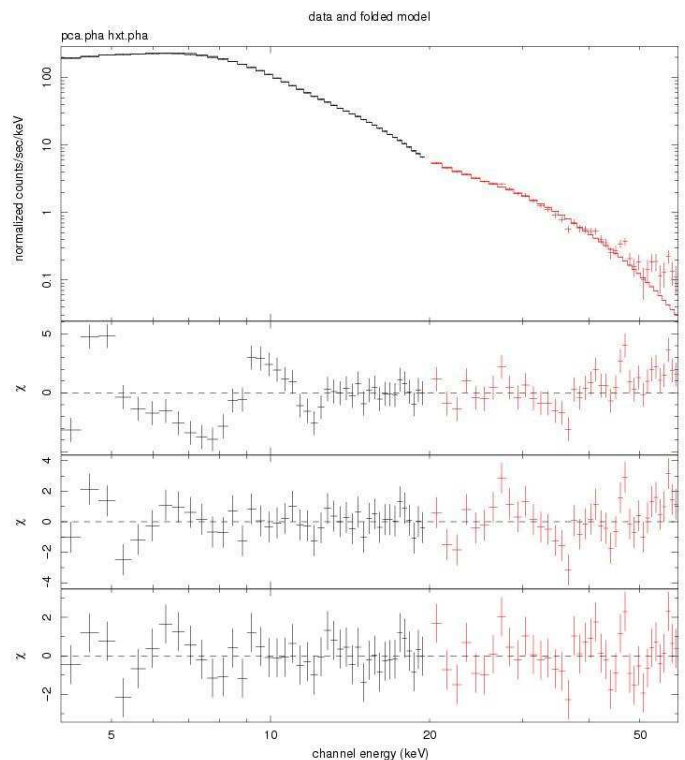


FIG. 15: The best-fit model (spectrum of 1999-03-20) after taking the 1st harmonic CRSF into consideration. The accessory residuals (the *top* of the  $\chi$ -plots) emphasize the presence of the third line (*bottom*) and show the special hump around 10 keV, which is modeled with a Gaussian (*middle*).

in a roughly power-law continuum with exponential cut-off at an energy  $E_c$  that is characteristic for the scattering electrons. Thus, in general continuum spectra of accreting binaries are modeled with a power-law with exponential cutoff. Following Nakajima et al. (2006), who used the Negative Positive Exponential Model (NPEX)  $NPEX(E) = (A_1 E^{-\alpha_1} + A_2 E^{+\alpha_2}) \exp(-E/kT)$ , in this project the sum out of a positive and a negative power-law was multiplied with the hightecut model, given by

$$hightecut(E) = \begin{cases} \exp\left(\frac{E_c - E}{E_f}\right) & E \geq E_c \\ 1 & E \leq E_c \end{cases}$$

was chosen to approximate the continuum. Here  $E_c$  is the cutoff energy and  $E_f$  the e-folding energy, both in keV (see [11]). The total continuum model  $M(E)$  is written as

$$M(E) = (A_1 E^{-\alpha_1} + A_2 E^{+\alpha_2}) \cdot hightecut(E), \quad (25)$$

where  $A_1, A_2$  denote the norm in units photons  $s^{-1} cm^{-2} keV^{-1}$  at 1 keV and  $\alpha_1, \alpha_2$  are the photon indices. In the following  $\alpha_2$  was fixed at 2.0, as did Nakajima et al. (2006), so that the positive power-law describes a Wien peak.

CSRFs were modeled with a Lorentzian shape by using the multiplicative model component *cyclabs*. To allow

also non-equidistant line-spacing, as discovered by Heindl et al. (1999), the depth of the additional harmonic line was fixed at zero. So each CRSF with energy  $E_{\text{cycl}}$ , width  $W$  and depth  $\tau$  is described itself by one *cyclabs* component and contributes to the shape of the resulting model the factor:

$$\text{cyclabs}(E) = \exp\left(-\tau \frac{(WE/E_{\text{cycl}})^2}{(E - E_{\text{cycl}})^2 + W^2}\right) \quad (26)$$

An interesting phenomenon in the spectrum analysis of many accreting neutron stars occurs at energies between 8 and 13 keV [1]: A small hump that cannot be explained yet can be seen in the spectrum. This feature was approximated with an additive *gaussian* component  $\text{gaussian}(E) = K/\sigma\sqrt{2\pi}\exp(-(E - E_l)^2/2\sigma^2)$  with line energy  $E_l$ , line width  $\sigma$  (both in keV) and norm  $K$ .

## B. Analysis

During the 1999 outburst 44 pointing observations of 4U 0115+63 were made with PCA and HEXTE. In this project 36 spectra out of these were chosen and fitted with a model consisting of (mostly) three CRSFs influencing the continuum model and an additional gaussian feature to describe the hump around 10 keV (see Fig.13). The occurring residuals after first fitting the data with the continuum model alone (see fig. 14 and fig. 15), then taking step by step one additional feature into account, justify this procedure. The main interest of the project lies in the 2004 outburst. However, there were only five pointing observations of PCA and HEXTE available. The same model used for the 1999 outburst was also applied to the 2004 outburst.

## C. Results

First one has to test whether the derived results, listed in table ?? and table ??, of 1999 outburst are consistent with the previous analysis of Nakajima et al. (2006). The fundamental cyclotron energies of the 1999 outburst are slightly below the results of Nakajima et al. (2006). The difference could arise from taking into account the unknown feature around 10 keV in this paper, what could result in a small shift of the harmonic CRSF to lower energies. Furthermore Nakajima et al. (2006) used equidistant spacing for the CRSFs. Thus the data can be considered to be consistent with those of Nakajima et al. (2006).

### 1. Comparison of 2004 outburst with 1999 outburst

As the data as well as the plots show the fundamental cyclotron line energy during the 2004 outburst of 4U 0115+63 behaves exactly in the same way as during the former outburst (see Figures (16)-(19)). No hysteresis could be observed.

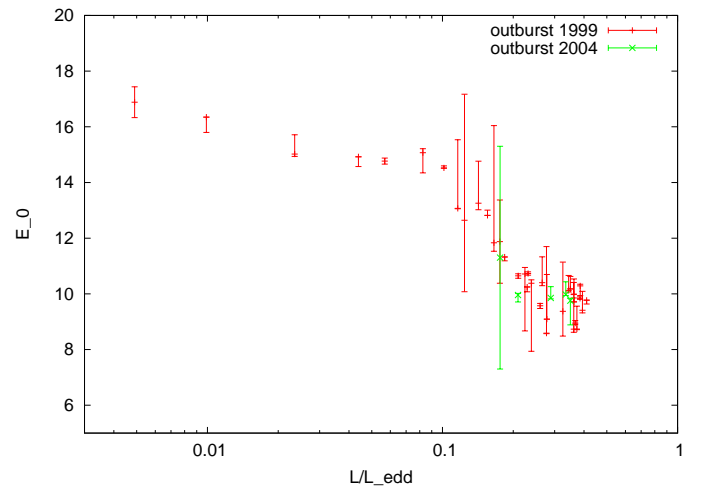


FIG. 16: Obtained fundamental cyclotron energies for 1999 outburst and 2004 outburst of 4U 0115+63. There is no difference in the behavior of the two outbursts. Besides, note the strong change in slope around  $L/L_{\text{edd}} \approx 0.1$ , what indicates different behavior of the accretion column.

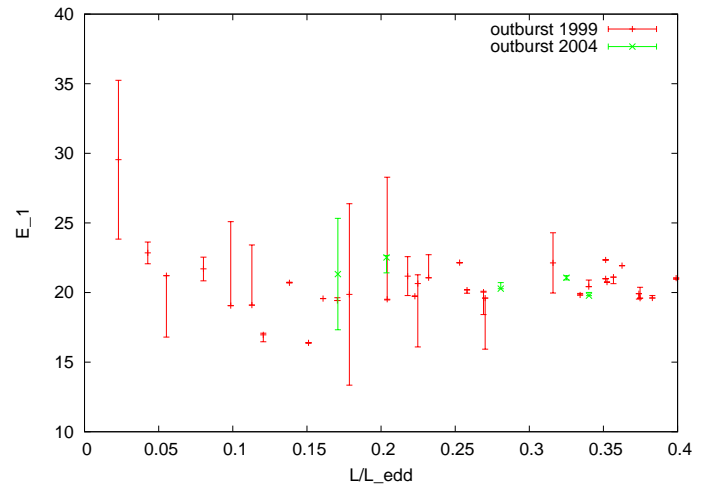


FIG. 17: Dependence of the first harmonic cyclotron energy on luminosity, again plotted for both outbursts. Except for quite low luminosities the energy remains constant.

In all of the plots the luminosity  $L$  is calculated at 7 kpc and plotted in units of  $L_{\text{edd}}$ , assuming a mass of the neutron star of  $1.4M_{\odot}$ .

Fig. (16) and Fig. (17) show the dependence of the fundamental and 1st harmonic cyclotron energy on the luminosity. While the fundamental cyclotron energy decreases strongly with increasing luminosity, the 1st harmonic cyclotron energy remains constant (for  $L/L_{\text{edd}} > 0.1$ ). One clearly recognizes that the slope of both energies is changing around  $L/L_{\text{edd}} \approx 0.1$ , what gives rise to the assumption that the physics of the accretion column is changing within this range.

Nakajima et al. (2006) emphasized the correlation of  $\tau$  and the  $W/E$  ratio among all the correlations of other pa-

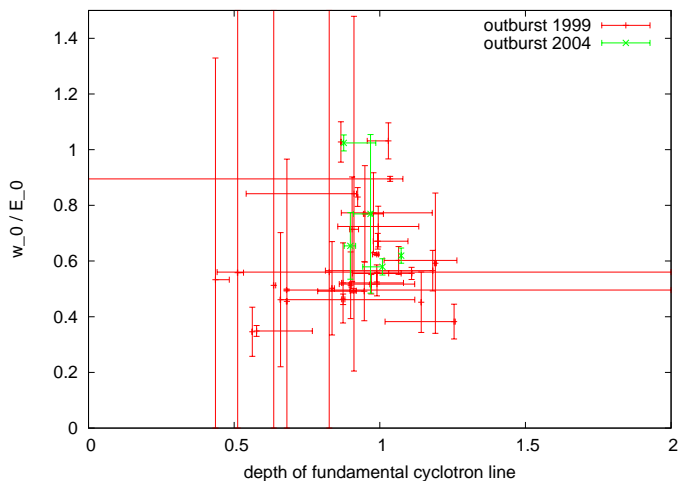


FIG. 18: A positive correlation can be found between the  $W_0/E_0$  ratio of the fundamental cyclotron line and its depth  $\tau_0$ .

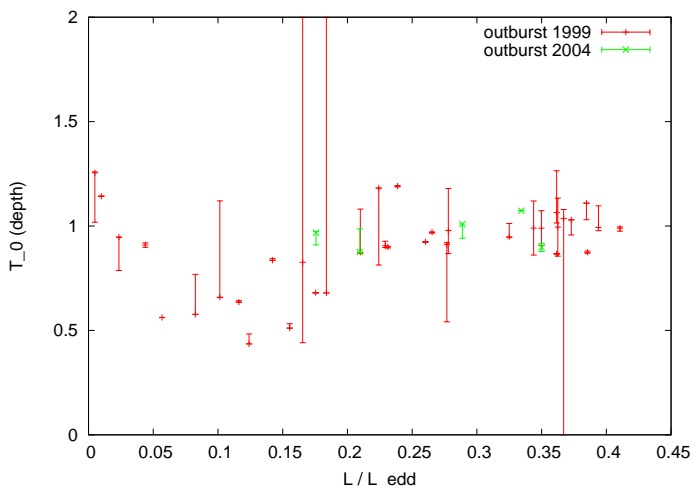


FIG. 19: The plot shows the depth of the fundamental CRSF versus luminosity. The minimum around  $L/L_{\text{edd}} > 0.1$  might also be a sign for a change in the accretion column. However, since the results of Nakajima et al. (2006) show a contradictory behavior, one has to examine it more closely.

rameters and so this relation is also presented in Fig. 18. Besides the huge errorbars one recognizes like Nakajima et al. (2006) a positive correlation between the fundamental width and its depth.

An interesting feature occurs when plotting the depth of the fundamental CRSF versus luminosity. It looks as if a minimum arises just around  $L/L_{\text{edd}} \approx 0.1$ . This might also indicate a change in the behavior of the accretion column. However, the results of Nakajima et al. (2006) show a contradictory behavior, the values of  $\tau_0$  are even increasing in this region. Thus, one has to examine it more closely. In this paper as well as by Nakajima et al. (2006) simple Lorentzians are used for approximating CRSFs, although generally it is known that the profile of the fun-

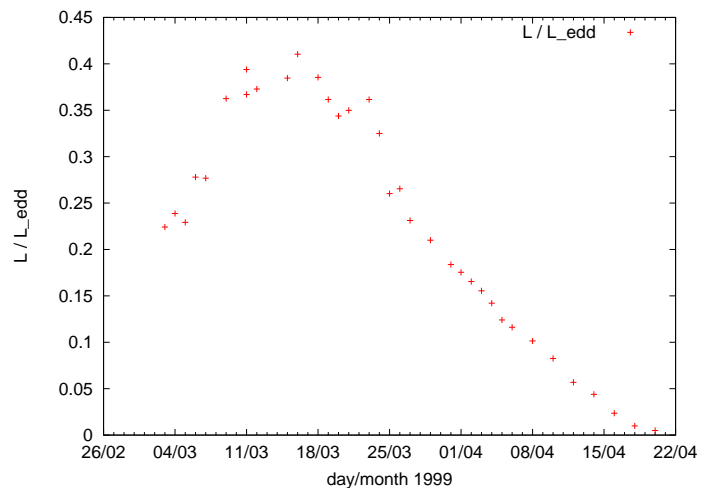


FIG. 20: The luminosity directly depends on the accretion rate at the NS. Here, the luminosity dependence on time is plotted.

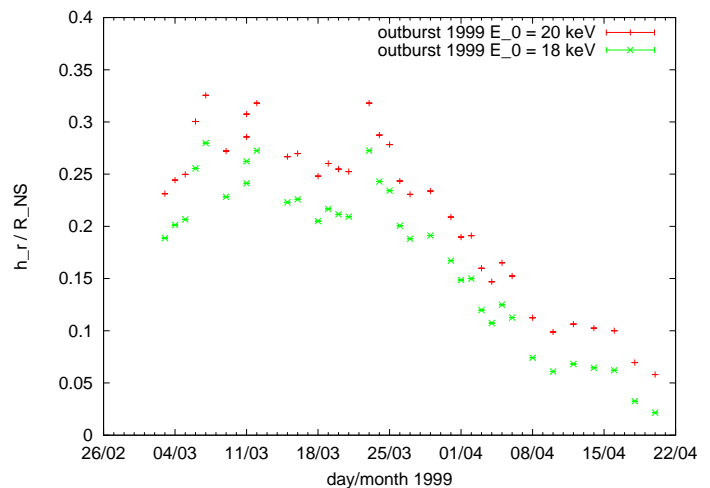


FIG. 21: Another hint for a possible change from super- to sub-Eddington accretion gives the rough change of the calculated height of the scattering region.

damental line exhibits a complex shape [17]. So perhaps using the results of Schoenherr et al. (2007), who developed a model for CRSFs, one is able to find about the real dependence of the depth on luminosity.

## 2. The height of the scattering region versus luminosity

Many authors (e.g. Staubert et al. (2007), Nakajima et al. (2006), Nelson et al. (1993)) gave attention to the physics in the accretion regime. As already mentioned in chap. VI it must be distinguished between sub- and super-Eddington accretion, whereas the decisive parameter is the local Eddington rate at the neutron star [19]. Since clear changes of parameters like the energies of CRSFs with the luminosity (see Fig. s (16), (17)) or the

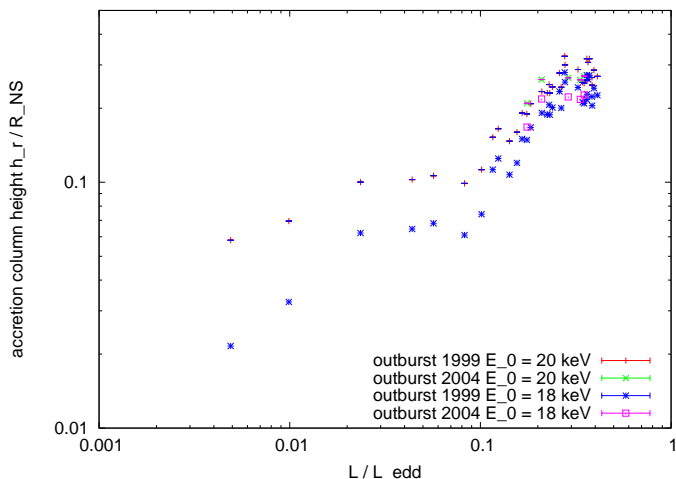


FIG. 22: Relative accretion column height  $h_r$  in dependence of luminosity. Clearly visible is a change in the accretion column at  $L/L_{\text{edd}} = 0.1$ .

height of the scattering region with time (see Fig. 21) and therefore with luminosity (compare Fig. 20) arise in the analysis of the 1999 outburst, one could take a possible transition from super- to sub-Eddington accretion into consideration. Therefore the height of the scattering region is examined more closely, because this value has to depend sufficiently on a possible relevant radiation pressure. It can be calculated approximately with the formula (19), derived in chap. VI:

$$\frac{h_r}{R_{\text{NS}}} = \left(\frac{E}{E_0}\right)^{-1/3} - 1. \quad (27)$$

Since the cyclotron line energy  $E_0$  directly at the NS surface is not known at all, it is followed Nakajima et al. (2006) and thus also two different values of  $E_0$ , 18 and 20 keV are employed. As predicted, the height  $h_r$  (see Fig. 22) changes its slope around  $L/L_{\text{edd}} \approx 0.1$ , where the possible transition point is assumed to be.

This luminosity-dependence of the  $h_r$  is compared in the following with the theory of super- and sub-Eddington accretion, presented in chap. VI. In the case of *super-Eddington* accretion Burnard et al. (1991) found the relation (24):

$$\frac{h_{\text{top}}}{R_{\text{NS}}} \approx \frac{L}{L_{\text{edd}} H_{\parallel}} \approx \frac{L}{1.23 L_{\text{edd}}} \quad (28)$$

Staubert et al. (2007) derived the relation (23) in the *sub-Eddington* accretion regime:

$$\frac{\Delta r}{R_{\text{NS}}} = -\frac{1}{3} \frac{\Delta E}{E} = -\frac{l_*}{R_{\text{NS}}} \frac{\Delta \dot{M}}{M} = -\frac{l_*}{R_{\text{NS}}} \frac{\Delta L}{L}. \quad (29)$$

Thus Staubert et al. (2007) predicted that the fractional change in cyclotron line energy is directly proportional to the fractional change in luminosity. Testing this relation on the data of the 1999 outburst with the fractional

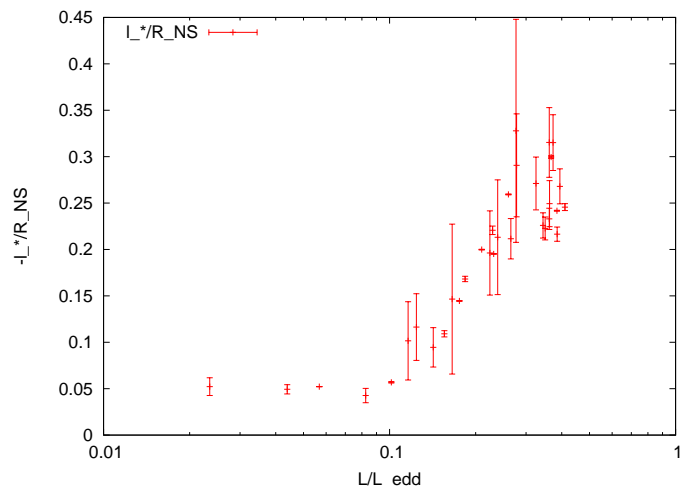


FIG. 23: Staubert et al. (2007) predicted a constant fractional change in the cyclotron line energy with a fractional change in luminosity.  $l_*/R_{\text{NS}} = 1/3 \cdot \Delta E/E \cdot L/\Delta L$  is plotted against luminosity.

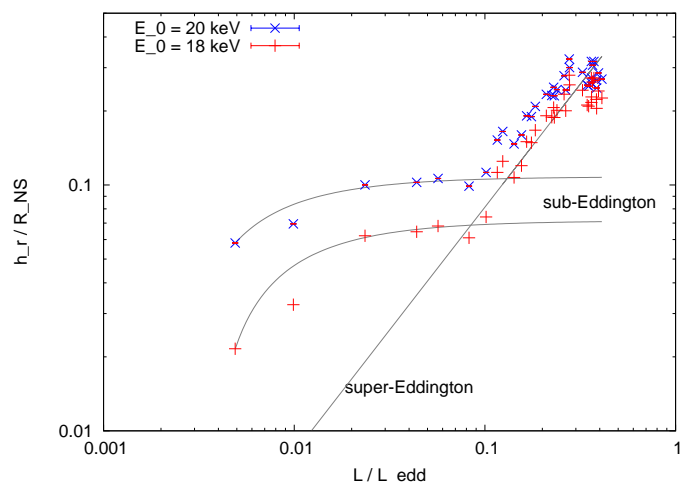


FIG. 24:  $h_r$  in comparison with the theoretical models for sub- and super-Eddington accretion

changes relating to the luminosity  $L_r$  and energy  $E_r$  of the observation in April 20 ( $\Delta L = L - L_r$ ,  $\Delta E = E - E_r$ ,  $E_r$ ,  $L_r$  of observation in April 20) yields Fig. 23. The prediction is verified at low luminosities,  $|l_*/R_{\text{NS}}| \approx 0.05$  is constant until  $L/L_{\text{edd}} \approx 0.1$ , then deviations occur since  $l_*/R_{\text{NS}}$  is increasing. For Her X-1 Staubert et al. (2007) derived  $l_*/R_{\text{NS}} \sim 0.01$ . Using  $-l_*/R_{\text{NS}} \approx 0.05$  and (29) the height of the scattering region can be expressed by:

$$\frac{h_r}{R_{\text{NS}}} = h_0 + 0.05 \frac{\Delta L}{L}, \quad (30)$$

where  $h_0 = h_r(L_r)$  calculated with (19) denotes the height of the scattering region on April 20.

Equations (28) and (30) are expressions for a theoretical approach for the height of the scattering region for super- and sub-Eddington accretion. Except for a

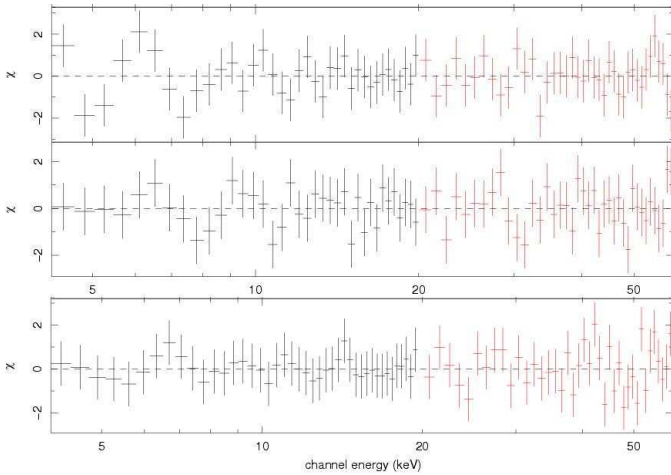


FIG. 25: Some spectra of 1999 outburst seem to have an excess at the energy of 6.4 keV that might indicate a Fe-K-line. The spectra in the figure are from top to bottom from observations of March 24, April 2, March 19.

saturation toward the highest luminosity (see also [3]) the two theories describe the height, calculated out of observed quantities, very good. This strengthens on the one hand the assumption that the observed cyclotron energy changes are due to changes of the scattering height  $h_r$  and on the second hand the transition from super- to sub-Eddington transition.

#### D. Observation of a Fe-K-line?

Although Nakajima et al. (2006) as well as Heindl et al. (1999) reported no detection of a Fe-K-line in the spectra of 1999 outburst, the residuals of some spectra exhibit at least a little excess around 6.4 keV (see Fig. 25, as well as Fig. 26 for the 2004 outburst) after fitting with the model described in the chapter above. To judge whether the spectrum contains a Fe-K-line one would have to do Monte Carlo simulation. However, within the scope of that project only the F-statistic of the new best-fit-models of spectra with the clearest excess was calculated and listed in table II and table III. The F-statistic gives the probability that the new best-fit  $\chi^2$  is achieved statistically [11]. But one has to be careful with interpreting the value, since Protassov et al. (2002) warned that the F-statistic is not sufficient good to test the presence of an emission or absorption line.

Taking on the one hand the high F-statistic results, but on the other hand the number of spectra with a little excess at the Fe-K-line energy into consideration, one really will have to do Monte Carlo simulation to be sure about the line.

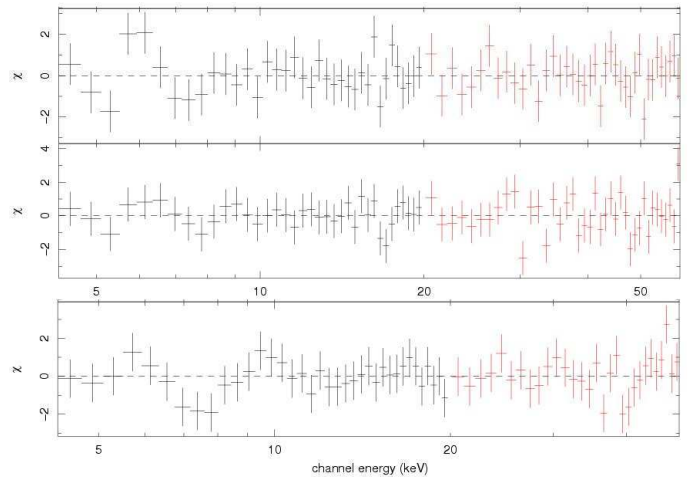


FIG. 26: Also the residuals of some spectra of the September–October outburst in 2004 show a little hump at 6.4 keV. The spectra in the figure are from top to bottom from observations of Sept. 6, Sept. 14 and Oct. 10.

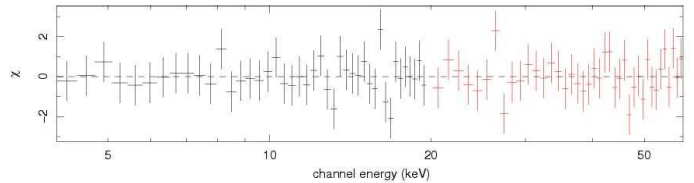


FIG. 27: The figure shows a counterexample for the observation of a Fe-K-line in all spectra (spectrum from 1999-03-06).

## VIII. CONCLUSION

This project shows that the 2004 outburst of 4U 0115+63 behaves in exactly the same way as the 1999 outburst. No hysteresis effect could be observed. Furthermore the theoretical approach for sub- and super-Eddington accretion describes the data of the March–April 1999 outburst of 4U 0115+63 very well, such that this indicates a transition from super- to sub-Eddington accretion during the 1999 outburst. However, it remains to be diagnosed whether there is a Fe-K-line present.

TABLE II:  
F-statistics of spectra taking an eventual Fe-K-line into account during 1999 outburst

Date (1999)	$E_{\text{Fe}}$ (keV)	ftest probability
Mar 19	6.56	0.35
Mar 24	6.1	1.7E-05
Apr 2	6.38	0.78

TABLE III:  
F-statistics of spectra taking an eventual Fe-K-line into account during 2004 outburst

Date (2004)	$E_{\text{Fe}}$ (keV)	f <sub>test</sub> probability
Sept 6	6.39	5.3E-04
Sept 14	6.40	0.23
Oct 2	5.9	0.61

### Acknowledgments

I would like to thank Prof. J. Wilms for taking much time for motivations, discussions, many explanations, constructive annotations, for answering trivial questions and for showing astronomy makes really fun. I am also grateful to all people working in the observatory in Bamberg for the great atmosphere during the three weeks of this project. Furthermore thanks to my parents for showing interest and especially thanks to my brother Tobias for demonstrating that even a seven-year-old boy is able to ask nontrivial questions about the sun and neutron stars.

### APPENDIX: BEST-FIT RESULTS

TABLE IV: The best-fit parameters of the date-sorted spectra of 2004 September–October outburst

Date	continuum spectrum			fundamental CRSF			1st harmonic CRSF		2nd harmonic CRSF		CRSF		gaussian	HEXTE	PCA	$\chi^2_{\text{red}}$				
	$A_1^a$	$\alpha_1$	$A_2^b$	$E_f$ (keV)	$E_0$ (keV)	$\tau_0$	$W_0$ (keV)	$E_1$ (keV)	$\tau_1$	$W_1$ (keV)	$E_2$ (keV)	$\tau_2$	$W_2$ (keV)	$E_l$ (keV)	$\sigma$ (keV)		Exposure (ks)	Exposure (ks)		
Sept 6	1.13	2.10	6.16	$5.25^{+0.09}_{-0.01}$	$9.96^{+0.06}_{-0.25}$	$0.88^{+0.11}_{-0.01}$	$10.20^{+0.47}_{-0.01}$	$22.52^{+0.13}_{-1.10}$	0.62	11.12	39.20	0.58	1.00	10.00	0.73	0.04	0.21	0.83	1.60	0.86
Sept 14	2.33	2.33	11.78	$5.07^{+0.16}_{-0.10}$	$9.75^{+0.99}_{-0.37}$	$0.90^{+0.02}_{-0.01}$	$6.38^{+1.13}_{-0.43}$	$19.78^{+0.23}_{-0.11}$	1.06	11.43	37.08	0.50	2.81	10.05	0.82	0.17	0.35	0.75	0.59	1.05
Sept 22	1.19	1.88	0.94	$5.48^{+0.10}_{-0.11}$	$9.97^{+0.63}_{-0.41}$	$1.07^{+0.01}_{-0.01}$	$6.18^{+0.44}_{-0.01}$	$21.06^{+0.15}_{-0.15}$	1.07	5.87	32.99	1.22	13.72	9.42	0.60	0.01	0.33	13.62	16.77	1.65
Sept 24	3.75	2.78	8.97	$5.38^{+0.11}_{-0.01}$	$9.85^{+0.41}_{-0.03}$	$1.01^{+0.01}_{-0.07}$	$5.71^{+0.01}_{-0.52}$	$20.28^{+0.43}_{-0.01}$	1.27	8.13	35.71	0.99	9.91	9.29	0.48	0.06	0.29	2.26	3.49	1.30
Oct 10	5.68	3.39	0.07	$4.65^{+0.06}_{-0.06}$	$11.30^{+4.00}_{-4.00}$	$0.97^{+0.01}_{-0.06}$	$8.70^{+0.94}_{-0.94}$	$21.33^{+4.00}_{-4.00}$	0.63	8.83	0.00	0.00	0.00	9.29	0.48	0.00	0.18	2.32	3.44	0.87

<sup>a</sup>in units photons  $\text{s}^{-1}\text{cm}^{-2}\text{keV}^{-1}$ <sup>b</sup>in units  $10^{-3}$  photons  $\text{s}^{-1}\text{cm}^{-2}\text{keV}^{-1}$ <sup>c</sup>in units photons  $\text{s}^{-1}\text{cm}^{-2}$ <sup>d</sup>calculated with  $M = 1.4M_{\odot}$ ,  $R = 7$  kpc according to eq.s (21), (8)

TABLE V: The best-fit parameters of the date-sorted spectra of 1999 March–April outburst

Date	continuum spectrum			fundamental CRSF			1st harmonic CRSF			2nd harmonic CRSF			gaussian			HEXTE	PCA			
	$A_1^a$	$\alpha_1$	$A_2^b$	$E_f$ (keV)	$E_0$ (keV)	$\tau_0$	$W_0$ (keV)	$E_1$ (keV)	$\tau_1$ (keV)	$W_1$ (keV)	$E_2$ (keV)	$\tau_2$	$W_2$ (keV)	$E_l$ (keV)	$\sigma$	$K^c$	$L/L_{\text{edd}}^d$	Exposure (ks)	Exposure $\chi^2_{\text{red}}$	
Mar 3	1.46	2.44	7.23	4.83 $^{+0.05}_{-0.30}$	10.71 $^{+0.23}_{-2.04}$	1.18 $^{+0.01}_{-0.37}$	6.06 $^{+0.88}_{-0.01}$	21.18 $^{+1.40}_{-0.01}$	0.93	6.18	32.31	0.77	7.95	12.41	2.14	1.92	0.22	0.34	0.59	0.78
Mar 4	1.84	2.51	7.39	5.17 $^{+0.38}_{-0.01}$	10.38 $^{+0.12}_{-2.44}$	1.19 $^{+0.01}_{-0.01}$	6.15 $^{+4.50}_{-0.50}$	21.06 $^{+1.66}_{-0.01}$	1.09	6.06	33.36	0.95	10.28	12.05	2.14	1.78	0.24	0.58	1.06	1.06
Mar 5	0.83	2.12	7.27	5.16 $^{+0.09}_{-0.32}$	10.25 $^{+0.01}_{-0.17}$	0.91 $^{+0.02}_{-0.01}$	7.31 $^{+1.93}_{-1.93}$	19.73 $^{+0.01}_{-0.01}$	1.04	9.28	36.03	0.48	6.94	9.72	0.55	0.12	0.23	0.84	0.08	0.97
Mar 6	10.12	3.99	10.3	5.41 $^{+10.00}_{-0.00}$	9.09 $^{+1.60}_{-0.01}$	0.98 $^{+0.20}_{-0.11}$	7.03 $^{+1.22}_{-1.08}$	19.60 $^{+0.01}_{-0.01}$	1.04	8.96	32.61	0.70	14.15	9.55	0.95	0.22	0.28	0.37	0.08	0.81
Mar 7	11.41	4.10	10.7	5.18 $^{+0.31}_{-0.31}$	8.59 $^{+3.11}_{-0.02}$	0.91 $^{+0.01}_{-0.37}$	7.23 $^{+10.62}_{-0.01}$	20.03 $^{+0.06}_{-0.61}$	1.22	10.09	37.74	0.51	6.07	11.25	1.79	1.72	0.28	0.59	0.14	0.76
Mar 9	2.68	2.57	12.1	5.34 $^{+1.08}_{-0.14}$	9.71 $^{+0.82}_{-0.03}$	0.99 $^{+0.14}_{-0.01}$	7.03 $^{+0.13}_{-0.16}$	20.75 $^{+0.01}_{-0.01}$	1.11	8.73	38.73	0.76	8.47	9.77	0.62	0.10	0.36	0.37	0.83	0.56
Mar 11	3.04	2.65	13.1	5.62 $^{+0.03}_{-0.03}$	9.41 $^{+0.09}_{-0.09}$	0.99 $^{+0.02}_{-0.02}$	6.32 $^{+0.11}_{-0.11}$	19.61 $^{+0.01}_{-0.01}$	1.27	10.23	38.19	0.82	11.56	9.85	0.96	0.28	0.39	0.89	1.84	0.73
Mar 11	20.77	4.29	13.9	5.45 $^{+10.00}_{-0.00}$	8.95 $^{+0.06}_{-0.82}$	1.04 $^{+0.04}_{-0.03}$	8.01 $^{+0.01}_{-0.10}$	21.11 $^{+0.47}_{-0.01}$	0.77	6.84	33.06	0.85	13.26	9.84	0.96	0.26	0.37	5.32	2.38	0.87
Mar 12	17.69	4.13	13.8	5.65 $^{+0.01}_{-0.10}$	8.73 $^{+0.02}_{-0.05}$	1.03 $^{+0.02}_{-0.01}$	9.01 $^{+0.05}_{-0.68}$	21.93 $^{+0.01}_{-0.01}$	0.63	5.09	33.32	0.93	13.16	9.67	0.80	0.17	0.37	15.4	15.58	1.19
Mar 15	2.54	2.54	2.13	5.56 $^{+0.39}_{-0.01}$	9.84 $^{+0.05}_{-0.04}$	1.11 $^{+0.01}_{-0.01}$	6.17 $^{+0.01}_{-0.43}$	19.92 $^{+0.01}_{-0.38}$	1.17	7.09	32.10	1.24	14.22	10.00	1.15	0.31	0.39	0.85	0.94	0.77
Mar 16	1.17	1.87	13.4	5.16 $^{+0.01}_{-0.01}$	9.77 $^{+0.01}_{-0.13}$	0.99 $^{+0.01}_{-0.01}$	5.47 $^{+0.01}_{-0.34}$	21.04 $^{+0.01}_{-0.02}$	1.19	8.40	35.03	0.75	9.28	10.00	1.09	0.23	0.41	0.42	0.50	1.12
Mar 18	1.11	1.79	12.4	4.77 $^{+10.00}_{-10.00}$	10.29 $^{+0.06}_{-0.35}$	0.87 $^{+0.01}_{-0.01}$	4.76 $^{+0.01}_{-0.01}$	19.59 $^{+0.79}_{-0.01}$	1.17	8.40	34.75	0.48	1.83	10.00	0.72	0.16	0.39	0.52	0.64	0.98
Mar 19	0.96	1.84	1.10	5.38 $^{+2.00}_{-0.50}$	9.99 $^{+0.42}_{-0.02}$	1.06 $^{+0.20}_{-0.05}$	6.02 $^{+0.48}_{-0.48}$	20.99 $^{+0.02}_{-0.01}$	1.17	6.67	34.03	1.09	12.65	9.61	0.67	0.13	0.36	2.47	2.99	0.71
Mar 20	0.99	1.79	9.86	5.46 $^{+0.01}_{-0.01}$	10.12 $^{+0.54}_{-0.05}$	0.99 $^{+0.13}_{-0.01}$	5.24 $^{+0.07}_{-0.73}$	19.82 $^{+0.11}_{-0.01}$	1.30	8.98	35.59	0.92	12.04	9.68	0.80	0.13	0.34	0.54	0.88	1.04
Mar 21	0.71	1.58	9.79	5.45 $^{+0.19}_{-0.19}$	10.18 $^{+0.45}_{-0.01}$	0.99 $^{+0.08}_{-0.01}$	5.65 $^{+0.00}_{-0.57}$	20.43 $^{+0.47}_{-0.01}$	1.25	8.19	35.85	0.98	12.31	9.68	0.66	0.10	0.35	3.24	3.17	0.58
Mar 23	0.67	1.86	9.87	5.79 $^{+0.09}_{-0.04}$	8.73 $^{+1.12}_{-0.11}$	0.87 $^{+0.01}_{-0.01}$	8.98 $^{+0.08}_{-0.92}$	22.34 $^{+0.02}_{-0.01}$	0.61	3.07	32.69	0.97	13.06	9.02	0.43	0.03	0.36	3.04	2.53	1.37
Mar 24	0.40	1.75	8.27	5.69 $^{+0.11}_{-0.56}$	9.37 $^{+1.77}_{-0.89}$	0.95 $^{+0.06}_{-0.01}$	7.21 $^{+2.17}_{-0.01}$	22.13 $^{+2.17}_{-0.01}$	0.84	5.87	34.66	1.00	11.80	11.93	1.99	0.63	0.33	1.44	0.19	0.90
Mar 25	0.50	1.77	7.22	5.43 $^{+0.05}_{-0.82}$	9.57 $^{+0.05}_{-0.93}$	0.92 $^{+0.01}_{-0.01}$	7.95 $^{+0.01}_{-0.48}$	22.15 $^{+0.02}_{-0.02}$	0.82	5.16	34.66	0.85	8.67	9.17	0.47	0.03	0.26	3.88	4.96	1.48
Mar 26	0.73	2.00	0.57	6.14 $^{+0.89}_{-0.06}$	10.40 $^{+0.11}_{-0.11}$	0.97 $^{+0.01}_{-0.01}$	5.37 $^{+0.01}_{-0.48}$	20.17 $^{+0.02}_{-0.02}$	1.46	7.86	36.46	1.53	12.90	11.96	7.07	0.94	0.27	0.54	0.30	1.51
Mar 27	49.68	5.70	4.08	5.85 $^{+0.02}_{-0.45}$	10.73 $^{+0.06}_{-0.06}$	0.90 $^{+0.01}_{-0.01}$	5.51 $^{+2.56}_{-0.01}$	20.64 $^{+0.63}_{-0.01}$	1.22	6.92	34.18	1.10	14.45	10.12	7.02	1.62	0.23	3.24	0.88	1.02
Mar 29	1.07	2.45	0.39	5.74 $^{+4.97}_{-0.01}$	10.65 $^{+0.09}_{-0.01}$	0.87 $^{+0.21}_{-0.01}$	5.55 $^{+3.06}_{-0.01}$	19.52 $^{+8.77}_{-0.01}$	1.22	7.75	33.24	1.02	14.11	11.59	6.88	0.99	0.21	3.26	4.06	1.10
Mar 31	1.16	2.84	3.08	5.31 $^{+2.83}_{-0.34}$	11.32 $^{+0.01}_{-0.13}$	0.68 $^{+1.77}_{-0.01}$	5.62 $^{+0.02}_{-0.01}$	19.87 $^{+6.52}_{-0.01}$	1.23	9.38	37.63	0.59	4.58	11.59	6.61	1.70	0.18	3.42	2.64	1.10
Apr 1	1.46	3.11	2.97	5.07 $^{+3.99}_{-5.07}$	11.88 $^{+1.50}_{-4.21}$	0.68 $^{+0.01}_{-0.39}$	5.41 $^{+12.06}_{-0.01}$	19.43 $^{+0.20}_{-0.01}$	1.08	8.50	36.57	0.40	7.82	11.47	6.78	1.83	0.18	0.44	0.72	1.12
Apr 2	1.13	2.84	0.16	6.84 $^{+10.00}_{-0.01}$	11.84 $^{+4.21}_{-0.31}$	0.83 $^{+13.69}_{-0.01}$	6.63 $^{+36.61}_{-0.01}$	19.57 $^{+0.01}_{-0.01}$	1.23	9.07	35.75	1.74	17.08	9.76	6.64	1.00	0.17	2.97	1.84	0.77
Apr 3	2.31	3.48	1.84	5.61 $^{+6.18}_{-4.60}$	12.82 $^{+0.19}_{-0.01}$	0.51 $^{+0.02}_{-0.01}$	7.15 $^{+91.14}_{-0.01}$	16.38 $^{+0.01}_{-0.01}$	0.83	13.64	40.46	0.57	3.54	10.77	5.73	1.56	0.16	0.53	0.37	1.17
Apr 4	1.35	3.06	2.27	5.37 $^{+0.79}_{-5.37}$	13.26 $^{+1.51}_{-0.23}$	0.84 $^{+0.01}_{-0.01}$	6.66 $^{+4.36}_{-0.01}$	20.70 $^{+0.05}_{-0.01}$	1.00	9.10	34.95	0.84	8.98	9.72	6.62	0.95	0.14	2.93	1.71	0.73
Apr 5	1.83	3.49	0.13	5.72 $^{+2.27}_{-2.27}$	12.64 $^{+4.53}_{-2.57}$	0.44 $^{+0.05}_{-0.01}$	6.74 $^{+19.76}_{-0.02}$	16.96 $^{+0.12}_{-0.50}$	0.94	13.86	36.94	1.08	1.21	11.64	5.85	1.67	0.12	0.62	0.91	0.73
Apr 6	0.98	2.93	1.70	5.1 $^{+0.64}_{-0.76}$	13.07 $^{+2.47}_{-0.01}$	0.64 $^{+0.01}_{-0.01}$	6.70 $^{+35.14}_{-0.01}$	19.10 $^{+4.32}_{-0.01}$	0.77	9.10	30.21	0.64	9.00	9.92	5.51	0.95	0.12	3.09	2.62	0.91
Apr 8	0.66	2.72	1.74	4.55 $^{+0.32}_{-0.32}$	14.53 $^{+0.02}_{-0.02}$	0.66 $^{+0.06}_{-0.01}$	6.70 $^{+2.00}_{-1.50}$	19.06 $^{+0.03}_{-0.03}$	0.65	9.01	0	0	1	9.92	5.52	0.88	0.10	3.35	3.70	1.11
Apr 10	0.58	2.84	0.24	4.34 $^{+1.67}_{-1.58}$	15.07 $^{+0.73}_{-0.11}$	0.58 $^{+0.10}_{-0.01}$	5.26 $^{+6.50}_{-0.60}$	21.70 $^{+0.85}_{-0.86}$	0.76	7.30	0	0	1	9.46	5.50	0.89	0.08	3.08	4.30	0.73
Apr 12	0.42	2.70	0.13	4.01 $^{+1.58}_{-0.40}$	14.77 $^{+0.11}_{-0.11}$	0.56 $^{+0.01}_{-0.01}$	5.11 $^{+2.60}_{-0.01}$	21.21 $^{+0.01}_{-0.41}$	0.65	5.99	0	0	1	9.20	6.45	0.64	0.06	3.51	4.77	0.92
Apr 14	0.17	1.46	0.49	3.8 $^{+0.08}_{-0.01}$	14.92 $^{+0.01}_{-0.35}$	0.91 $^{+0.01}_{-0.01}$	7.36 $^{+0.01}_{-0.13}$	22.85 $^{+0.78}_{-0.78}$	0.60	2.98	0	0	1	0	0	0	0.04	2.97	4.08	0.85
Apr 16	0.12	1.47	0.01	3.93 $^{+10.00}_{-0.49}$	15.02 $^{+0.08}_{-0.08}$	0.95 $^{+0.01}_{-0.01}$	7.39 $^{+1.74}_{-1.43}$	29.54 $^{+5.70}_{-5.70}$	2.10	3.92	0	0	1	0	0	0	0.02	0.54	0.85	1.11
Apr 18	0.00	1.47	0.03	4.24 $^{+0.11}_{-0.10}$	16.35 $^{+0.08}_{-0.55}$	1.14 $^{+0.01}_{-0.01}$	7.39 $^{+3.47}_{-0.07}$	29.54 $^{+0.01}_{-0.01}$	0	1	0	0	1	0	0	0	0.01	0.54	0.83	0.99
Apr 20	0.01	1.47	4.3E-03	4.5 $^{+0.01}_{-0.69}$	16.88 $^{+0.55}_{-0.55}$	1.25 $^{+0.01}_{-0.24}$	6.46 $^{+2.07}_{-0.01}$	29.54 $^{+0.01}_{-0.01}$	0	1	0	0	1	0	0	0	4.91E-03	0.39	0.66	0.84
Apr 22	8.3E-05	1.53	6.6E-04	3.18 $^{+10.00}_{-10.00}$	17.38 $^{+92.01}_{-3.96}$	0.99 $^{+65.01}_{-19.22}$	11.19 $^{+0.01}_{-96.40}$	29.54 $^{+0.01}_{-0.01}$	0	1	0	0	1	0	0	0	1.03E-04	0.87	1.33	0.50

<sup>a</sup>in units photons s<sup>-1</sup>cm<sup>-2</sup>keV<sup>-1</sup><sup>b</sup>in units 10<sup>-3</sup> photons s<sup>-1</sup>cm<sup>-2</sup>keV<sup>-1</sup><sup>c</sup>in units photons s<sup>-1</sup>cm<sup>-2</sup><sup>d</sup>calculated with  $M = 1.4M_{\odot}$ ,  $R = 7$  kpc according to eq.s (21), (8)

- 
- [1] I. Kreykenbohm, Ph.D. thesis, Eberhard-Karls-Universität Tübingen (2004).
- [2] U. Geppert and V. Urpin, *mn* **271**, 490 (1994).
- [3] M. Nakajima, T. Mihara, K. Makishima, and H. Niko, *Astrophys. J.* **646**, 1125 (2006), astro-ph/0601491.
- [4] W. A. Heindl, W. Coburn, D. E. Gruber, M. R. Pelling, R. E. Rothschild, J. Wilms, K. Pottschmidt, and R. Staubert, *Astrophys. J., Lett.* **521**, L49 (1999), astro-ph/9904222.
- [5] W. A. Wheaton, J. P. Doty, F. A. Primini, B. A. Cooke, C. A. Dobson, A. Goldman, M. Hecht, S. K. Howe, J. A. Hoffman, and A. Scheepmaker, *Nature (London)* **282**, 240 (1979).
- [6] S. D. M. White, *mn* **189**, 831 (1979).
- [7] R. E. Rothschild, P. R. Blanco, D. E. Gruber, W. A. Heindl, D. R. MacDonald, D. C. Marsden, M. R. Pelling, L. R. Wayne, and P. L. Hink, *Astrophys. J.* **496**, 538 (1998), astro-ph/9710328.
- [8] K. Jahoda, J. H. Swank, A. B. Giles, M. J. Stark, T. Strohmayer, W. Zhang, and E. H. Morgan (1996), pp. 59–70.
- [9] A. M. Levine, H. Bradt, W. Cui, J. G. Jernigan, E. H. Morgan, R. Remillard, R. E. Shirey, and D. A. Smith, *Astrophys. J., Lett.* **469**, L33+ (1996), astro-ph/9608109.
- [10] URL <http://xte.mit.edu/asmlc/ASM.html>.
- [11] *XSPEC User's Guide version 12.3.1* (2007).
- [12] W. H. Press and B. P. Flannery, *Numerical Recipes* (Cambridge University Press, 1992).
- [13] L. Bildsten, D. Chakrabarty, J. Chiu, M. H. Finger, D. T. Koh, R. W. Nelson, T. A. Prince, B. C. Rubin, D. M. Scott, M. Stollberg, et al., *ApJS* **113**, 367 (1997), astro-ph/9707125.
- [14] A. K. Harding and D. Lai, *Reports of Progress in Physics* **69**, 2631 (2006), astro-ph/0606674.
- [15] L. D. Landau and E. M. Lifshitz, *Quantum Mechanics* (Pergamon Press: New York, 1977).
- [16] M. H. Johnson and B. A. Lippmann, *Physical Review* **76**, 828 (1949).
- [17] G. Schoenherr, J. Wilms, P. Kretschmar, A. Kreykenbohm, A. Santangelo, R. E. Rothschild, W. Coburn, and R. Staubert, *A&A* (2007).
- [18] R. W. Nelson, E. E. Salpeter, and I. Wasserman, *Astrophys. J.* **418**, 874 (1993).
- [19] R. Staubert, N. I. Shakura, K. Postnov, J. Wilms, R. E. Rothschild, W. Coburn, L. Rodina, and D. Klochkov, *Astronomy & Astrophysics* **465**, L25 (2007), astro-ph/0702490.
- [20] D. J. Burnard, J. Arons, and R. I. Klein, *Astrophys. J.* **367**, 575 (1991).
- [21] R. Protassov, D. A. van Dyk, A. Connors, V. L. Kashyap, and A. Siemiginowska, *Astrophys. J.* **571**, 545 (2002), astro-ph/0201547.